

2-D Analytical Prediction of Eddy Currents, Circuit Model Parameters, and Steady-State Performances in Solid Rotor Induction Motors

Kamel Boughrara¹, Frédéric Dubas², and Rachid Ibtouen³

¹Université de Khemis-Miliana, Laboratoire de l'Energie et des systèmes intelligents,
Route de Theniet El-had, Khemis-Miliana, 44225, Algeria

²Department of Energy, FEMTO-ST Institute, University of Franche-Comté, Belfort 90000, France

³Ecole Nationale Polytechnique, Laboratoire de Recherche en Electrotechnique,
10, av. Pasteur, El Harrach, Algiers 16200, Algeria

This paper presents a 2-D analytical method in the complex domain for the computation of magnetic field distribution, eddy currents, circuit model parameters, and steady-state performances in solid rotor induction motors. The proposed static analytical model considers stator slotting with tooth-tips. The rotor motion is simulated by varying the slip. The analytical magnetic field distribution is computed in polar coordinates from 2-D subdomain method (i.e., based on the formal resolution of Maxwell's equations applied in subdomain) in each region, i.e., semiclosed stator slots, air gap, solid rotor, and shaft. The electromagnetic torque is obtained from both the electrical equivalent circuit and Maxwell stress tensor that is given by the magnetic field distribution. Analytical results are validated by the static finite-element method.

Index Terms—Circuit model parameters, eddy currents, induction motors, slotted stator, subdomain method, tooth-tips.

I. INTRODUCTION

SOLID ROTOR induction motors become more preferable for the high-speed machines because of their advantages of the mechanical strength and robust construction [1]. Thus, analysis and optimization are the main concern of a motor designer in these motors. In the literature, there are many induction machine models that have been developed over the years. Numerical (e.g., the finite elements or the finite differences), equivalent circuits (i.e., magnetic, electrical, and/or thermal), and (semi) analytical methods are the most used. Numerical method has proven to be efficient when dealing with complicated geometries. Its solution is precise and considers the nonlinear materials of the machine, but it is time-consuming [2]–[15]. There are many numerical models for the calculation of magnetic field, electrical equivalent circuit (EEC) parameters, and electromagnetic performances. In the step-by-step numerical methods, the magnetic field distribution is obtained with considering rotor motion. The static numerical methods predict magnetic field and EEC parameters with considering the locked rotor. The rotor motion is simulated by varying the slip. Compared with numerical methods, the magnetic equivalent circuit (MEC), i.e., reluctance network method, consider the real structure (e.g., slotted stator with tooth-tips,...) and nonlinear material with lesser time of computation [16]. However, the numerical method is more accurate than nonlinear adaptive MEC. To improve the accuracy of the MEC, many authors proposed its coupling with numerical or the analytical method [17]. Analytical method based on

the resolution of Maxwell's equations is the most preferred method by designer. It is very fast and precise and then it is always considered in optimization. However, actually it is limited to simple structures of solid rotor induction motors where stator semiclosed slots are not considered and the current density distribution of the m -phases is assumed distributed at the internal stator bore [18]–[25]. The analytical method is also coupled to numerical method to fasten the calculation time and for considering stator slotting [26]. Of course, there is no analytical method in the literature, which predict magnetic field in slotted solid rotor induction motor.

In this paper, a 2-D analytical prediction of magnetic field distribution, eddy currents, EEC parameters, and steady-state performances of solid rotor induction machines considering the stator slotting with tooth-tips is presented. It involves analytical resolution of partial differential equations in polar coordinates from Maxwell's equations in semiclosed stator slots, air gap, and conducting rotor and shaft. The proposed static analytical method in the complex domain is based on the sub-domain method, using the Fourier's series and the method of separation variables [27]–[31], and the principle that the time pulsation is ω in the stator and $s \cdot \omega$ in the rotor [2], [11], [12]. This model allows an accurate prediction of motor performances at any load condition without involving the rotor motion. The analytical results are then compared with those found by static finite-element method (FEM) [32].

II. PROBLEM FORMULATION AND ASSUMPTIONS

Fig. 1 shows the machine model where Region I represents the air gap, Region II the conducting rotor, Regions III and IV the stator semiclosed slots, and Region V a conducting shaft. The 2-D analytical model in polar coordinates is formulated in vector potential with the following assumptions.

Manuscript received March 20, 2014; revised May 30, 2014 and June 25, 2014; accepted July 21, 2014. Date of publication July 24, 2014; date of current version December 12, 2014. Corresponding author: K. Boughrara (e-mail: boughrarakamel@yahoo.fr).

Color versions of one or more of the figures in this paper are available online at <http://ieeexplore.ieee.org>.

Digital Object Identifier 10.1109/TMAG.2014.2342666

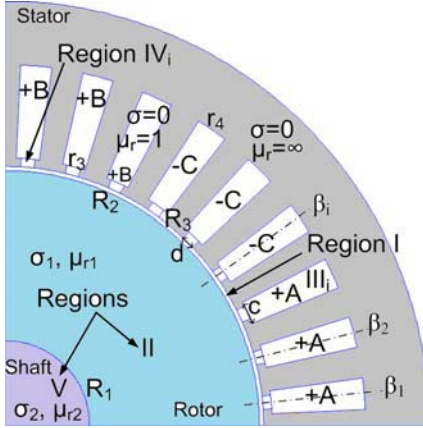


Fig. 1. Analyzed solid rotor induction motor with conducting rotor and shaft (one pole).

- 1) The end effects are neglected (i.e., the machine is infinitely long: the magnetic variables are independent of z).
- 2) The stator is assumed to be infinitely permeable (i.e., the saturation effect is neglected) with zero electrical conductivity.
- 3) The machine is supplied with a balanced three phase's sinusoidal currents.
- 4) The time variation of the magnetic field is assumed to be sinusoidal.
- 5) The relative magnetic permeability and electrical conductivity of solid rotor and shaft are assumed to be constant.
- 6) The ends of the rotor are equipotential surfaces so that the potential difference equal to zero.
- 7) The current density in the slots has only one component along the z -axis.
- 8) The resultant eddy-current densities in the solid rotor and shaft has only one component along the z -axis.
- 9) The stator semiclosed slots have radial sides, as shown in Fig. 1.

In this paper, the method principle is to start from the idea that the time pulsation is ω in the stator region and $\omega_{rm} = s \cdot \omega = \omega - p \cdot \Omega$ in the rotor region; where ω_{rm} represent the frequency of eddy currents in the rotor, s the slip, p the number of pole pairs, and Ω the constant angular velocity of rotor.

From the above assumptions, the magnetic vector potential $A(r, \theta)$ in each region is given by

$$\Delta A(r, \theta) = 0 \quad (1)$$

in Regions I and IV

$$\Delta A(r, \theta) = -\mu_0 \cdot J(r, \theta) \quad (2)$$

in Region III

$$\Delta A(r, \theta) = j \cdot \mu_0 \cdot \mu_r \cdot \sigma \cdot \omega_{rm} \cdot A(r, \theta) \quad (3)$$

in Regions II and V, where

$$A(r, \theta, t) = \Re{e} \{A(r, \theta)\} \cdot e^{j \cdot \omega \cdot t} \quad (4)$$

$$J(r, \theta, t) = \Re{e} \{J(r, \theta)\} \cdot e^{j \cdot \omega \cdot t} \quad (5)$$

in the stator (Regions I, III, and IV)

$$A(r, \theta, t) = \Re{e} \{A(r, \theta)\} \cdot e^{j \cdot \omega_{rm} \cdot t} \quad (6)$$

in the rotor (Regions II and V), $J(r, \theta) = J_i$ represents the current density in the stator slots, which is constant in each slot, μ_r and σ the relative permeability and electrical conductivity of the solid rotor and shaft, $j = \sqrt{-1}$ the complex number, and μ_0 the permeability of vacuum.

The field vectors \vec{B} and \vec{H} are coupled by

$$\vec{B}(r, \theta) = \mu_0 \cdot \mu_r \cdot \vec{H}(r, \theta). \quad (7)$$

The radial and tangential components of the magnetic flux density are deduced from $A(r, \theta)$ by

$$B_r(r, \theta) = \frac{1}{r} \cdot \frac{\partial A(r, \theta)}{\partial \theta} \quad (8a)$$

$$B_\theta(r, \theta) = -\frac{\partial A(r, \theta)}{\partial r}. \quad (8b)$$

III. MAGNETIC FIELD SOLUTIONS

The resolution of partial differential equations (1)–(3) using the method of separation variables, Fourier's series analysis, and boundary and interface conditions permits to determine magnetic field distribution in all regions.

A. Solution of Laplace's Equation in the Air Gap

In Region I, which is an annular domain situated between the radii R_2 and R_3 (Fig. 1), the solution of complex Laplace equation (1) is

$$A_I(r, \theta) = A_{10} + A_{20} \cdot \ln(r) + \sum_{n=1}^{\infty} (A_{1n} \cdot r^n + A_{2n} \cdot r^{-n}) \cdot \sin(n \cdot \theta) + \sum_{n=1}^{\infty} (A_{3n} \cdot r^n + A_{4n} \cdot r^{-n}) \cdot \cos(n \cdot \theta) \quad (9)$$

where n is the spatial harmonics orders (a positive integer), and A_{10} – A_{4n} are the complex integration constants in Region I.

B. Solution of Helmholtz's Equation in the Solid Rotor

The rotor is a cylindrical conductive region (i.e., Region II) situated between the radii R_1 and R_2 (Fig. 1). The solutions of diffusion equation (3) are given by

$$A_{II}(r, \theta) = A_{50} \cdot J_0(\alpha \cdot r) + A_{60} \cdot Y_0(\alpha \cdot r) + \sum_{n=1}^{\infty} \left(A_{5n} \cdot J_n(\alpha \cdot r) + A_{6n} \cdot Y_n(\alpha \cdot r) \right) \cdot \cos(n \cdot \theta) + \sum_{n=1}^{\infty} \left(A_{7n} \cdot J_n(\alpha \cdot r) + A_{8n} \cdot Y_n(\alpha \cdot r) \right) \cdot \sin(n \cdot \theta) \quad (10)$$

for $\alpha = (-j \cdot \mu_0 \cdot \mu_r \cdot \sigma \cdot \omega_{rm})^{1/2}$

$$A_{II}(r, \theta) = A_{50} \cdot I_0(\alpha \cdot r) + A_{60} \cdot K_0(\alpha \cdot r) + \sum_{n=1}^{\infty} \left(A_{5n} \cdot I_n(\alpha \cdot r) + A_{6n} \cdot K_n(\alpha \cdot r) \right) \cdot \cos(n \cdot \theta) + \sum_{n=1}^{\infty} \left(A_{7n} \cdot I_n(\alpha \cdot r) + A_{8n} \cdot K_n(\alpha \cdot r) \right) \cdot \sin(n \cdot \theta) \quad (11)$$

for $\alpha = (j \cdot \mu_0 \cdot \mu_r \cdot \sigma_1 \cdot \omega_{\text{rm}})^{1/2}$, where $A5_0$ – $A8_n$ are the complex integration constants in Region II, $J_n(\alpha \cdot r)$ and $Y_n(\alpha \cdot r)$ are the Bessel function of the first and second kinds of the order n , and $I_n(\alpha \cdot r)$ and $K_n(\alpha \cdot r)$ are the modified Bessel function of the first and second kinds of the order n . It is noticed that the solution (10) is used to predict magnetic field in the conductive rotor. Both formulations are mathematically correct and identical.

C. Solution of Poisson's Equation in the Stator Slots

Using the Fourier series analysis and the method of separation variables, the magnetic field prediction in the stator slots with single- or double-layer winding (Fig. 2) is calculated analytically by solving (2). These general solutions consider all types of multiphase and multipoles windings (integer or fractional slot per pole per phase).

1) Single-Layer Winding: The solution of (2) in the i th slot associated with the boundary conditions shown in Fig. 2(a) is given by

$$A_{III,i}(r, \theta) = C_{i,0} + \frac{1}{2} \cdot \mu_0 \cdot J_i \cdot r_4^2 \cdot \left[\ln(r) - \frac{1}{2} \cdot \left(\frac{r}{r_4} \right)^2 \right] + \sum_{k=1}^{\infty} C_{i,k} \cdot h_k(r) \cdot \cos \left(\frac{k\pi}{c} \cdot \left(\theta - \beta_i + \frac{c}{2} \right) \right) \quad (12a)$$

where k is the spatial harmonics orders (a positive integer), β_i the angular position of the i th slot, c the slot opening, $C_{i,0} \sim C_{i,k}$ are the complex integration constants in Region III, and

$$h_k(r) = \left[1 + \left(\frac{r}{r_4} \right)^{2 \cdot \frac{k\pi}{c}} \right] \cdot r^{-\frac{k\pi}{c}}. \quad (12b)$$

2) Double-Layer Winding (Left and Right Layer Coils): The slot contains two coils, as shown in Fig. 2(b). The Fourier's series expansion of the current density is given by

$$J_i(\theta) = J_{i,0} + \sum_{l=1}^{\infty} J_{i,l} \cdot \cos \left(\frac{l\pi}{c} \cdot \left(\theta - \beta_i + \frac{c}{2} \right) \right) \quad (13a)$$

with

$$J_{i,0} = \frac{e}{c} \cdot (J_{1i} + J_{2i}) \quad (13b)$$

$$J_{i,l} = \frac{2}{l\pi} \cdot \left[J_{1i} + (-1)^l \cdot J_{2i} \right] \cdot \sin \left(\frac{l\pi}{c} \cdot e \right) \quad (13c)$$

where J_{1i} and J_{2i} are the current densities of the corresponding i th coils with the thickness e .

Considering the boundary equations shown in Fig. 2(b), leads to the general solution of (2)

$$A_{III,i}(r, \theta) = C_{i,0} + \frac{1}{2} \cdot \mu_0 \cdot J_{i,0} \cdot r_4^2 \cdot \left[\ln(r) - \frac{1}{2} \cdot \left(\frac{r}{r_4} \right)^2 \right] + \sum_{l=1}^{\infty} \left(\begin{array}{l} C_{i,l} \cdot h_l(r) \\ + F_{i,l} \cdot r^{2 \cdot \frac{l\pi}{c}} \\ - G_{i,l} \cdot r^{\frac{l\pi}{c}} \end{array} \right) \cos \left(\frac{l\pi}{c} \cdot \left(\theta - \beta_i + \frac{c}{2} \right) \right) \quad (14a)$$

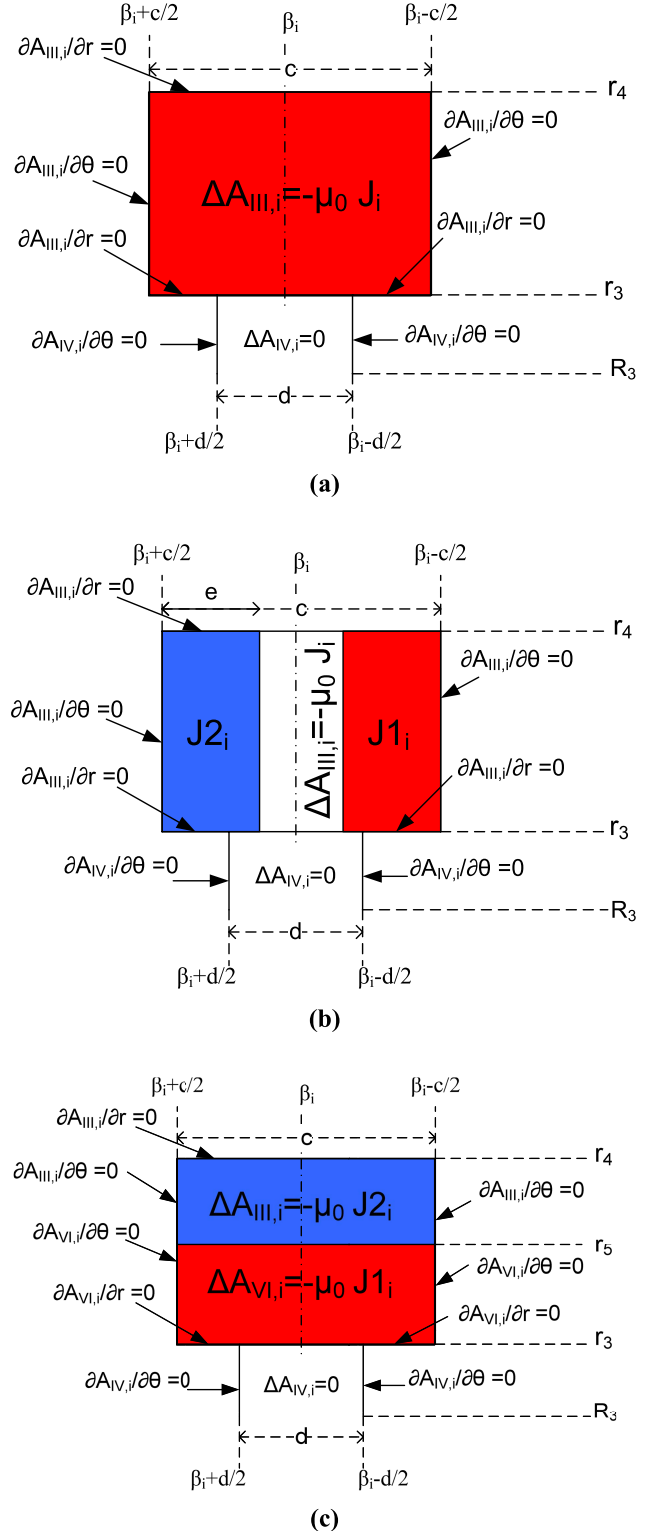


Fig. 2. i th stator semiclosed slot. (a) Single-layer winding. (b) Double-layer winding (left and right layers). (c) Double-layer winding (upper and lower layers).

where l is the spatial harmonics orders (a positive integer), $C_{i,l}$ is the complex integration constant in Region III, and

$$F_{i,l} = \mu_0 \cdot \frac{J_{i,l}}{\left(\frac{l\pi}{c} \right)^2 - 4} \quad (14b)$$

$$G_{i,l} = 2 \cdot F_{i,l} \cdot \frac{1}{\frac{l\pi}{c} \cdot r_4^{\frac{l\pi}{c}-2}}. \quad (14c)$$

The case $l\pi = 2c$ can be solved easily.

3) Double-Layer Winding (Upper and Lower Layer Coils):

The double-layer winding can be set as upper and lower layers, as shown in Fig. 2(c). The general form of magnetic vector potential in the coil represented by the current density $J2_i$ and associated with the boundary conditions shown in Fig. 2(c) is given by

$$\begin{aligned} A_{VI,i}(r, \theta) = & C1_{i,0} + C2_{i,0} \ln(r) - \frac{1}{4} \cdot \mu_0 \cdot J1_i \cdot r^2 \\ & + \sum_{h=1}^{\infty} \left[C1_{i,l} \cdot r^{-\frac{h\pi}{c}} \right. \\ & \left. + C2_{i,h} \cdot r^{\frac{h\pi}{c}} \right] \\ & \times \cos \left(\frac{h\pi}{c} \cdot \left(\theta - \beta_i + \frac{c}{2} \right) \right) \end{aligned} \quad (15)$$

where h is the spatial harmonics orders (a positive integer), and $C1_{i,0}$ – $C2_{i,h}$ are the complex integration constants in Region VI.

The general form of magnetic vector potential in the coil $J2_i$ [Fig. 2(c)] is given by (12).

D. Solution of Laplace's Equation in the Stator Semislots

In each stator semiclosed slot (i) of Region IV (Figs. 1 and 2), the solution of Laplace's equation (1) associated with the boundary conditions of Fig. 2 is given by

$$\begin{aligned} A_{IV,i}(r, \theta) = & A9_{i,0} + A10_{i,0} \cdot \ln(r) \\ & + \sum_{m=1}^{\infty} \left(A9_{i,m} \cdot r^{-\frac{m\pi}{d}} \right. \\ & \left. + A10_{i,m} \cdot r^{\frac{m\pi}{d}} \right) \\ & \times \cos \left(\frac{m\pi}{d} \cdot \left(\theta - \beta_i + \frac{d}{2} \right) \right) \end{aligned} \quad (16)$$

where m is the spatial harmonics orders (a positive integer), $A9_{i,0}$ – $A10_{i,m}$ are the complex integration constants in Region IV, and d the semislot opening.

E. Solution of Helmholtz's Equation in the Shaft

In the conducting shaft Region V (Figs. 1 and 2), the solutions of the complex Helmholtz's equation (3) are given by

$$\begin{aligned} A_V(r, \theta) = & A11_0 \cdot J_0(\lambda \cdot r) \\ & + \sum_{n=1}^{\infty} A11_n \cdot J_n(\lambda \cdot r) \cdot \cos(n \cdot \theta) \\ & + \sum_{n=1}^{\infty} A12_n \cdot J_n(\lambda \cdot r) \cdot \sin(n \cdot \theta) \end{aligned} \quad (17)$$

for $\lambda = \sqrt{-j \cdot \mu_0 \cdot \mu_{r2} \cdot \sigma_2 \cdot \omega_{rm}}$

$$\begin{aligned} A_V(r, \theta) = & A11_0 \cdot I_0(\lambda \cdot r) \\ & + \sum_{n=1}^{\infty} A11_n \cdot I_n(\lambda \cdot r) \cdot \cos(n \cdot \theta) \\ & + \sum_{n=1}^{\infty} A12_n \cdot I_n(\lambda \cdot r) \cdot \sin(n \cdot \theta) \end{aligned} \quad (18)$$

for $\lambda = (j \cdot \mu_0 \cdot \mu_{r2} \cdot \sigma_2 \cdot \omega_{rm})^{1/2}$, and $A11_0$ – $A12_n$ are the complex integration constants in Region V.

In the case of nonconducting shaft ($\sigma_2 = 0$), the solution of Laplace's equation in Region V can be obtained easily. In this paper, the solution (17) is used to predict magnetic field in the shaft region. However, (18) gives the same result as (17).

F. Interfaces Conditions

For single or double layer winding with left and right layer coils in the solid rotor induction motors, the 21 unknown constants in Fourier's series $A1_0$ – $A12_n$, $C_{i,0}$ – $C_{i,k}$, and $A9_{i,0}$ – $A10_{i,m}$ of magnetic field solutions in all regions, eight interfaces conditions should be introduced.

The interface conditions between Regions II and V at $r = R_1$ are

$$A_V(R_1, \theta) = A_{II}(R_1, \theta) \quad (19)$$

$$H_{V,\theta}(R_1, \theta) = H_{II,\theta}(R_1, \theta). \quad (20)$$

The interface conditions between Regions I and II at $r = R_2$ are

$$A_{II}(R_2, \theta) = A_I(R_2, \theta) \quad (21)$$

$$H_{II,\theta}(R_2, \theta) = H_{I,\theta}(R_2, \theta). \quad (22)$$

The interface conditions between Regions I and IV at $r = R_3$ are

$$A_I(R_3, \theta) = A_{IV,i}(R_3, \theta) \quad (23)$$

$$H_{I,\theta}(R_3, \theta) = H_{IV,\theta,i}(R_3, \theta). \quad (24)$$

The interface conditions between Regions III and IV at $r = r_3$ are

$$A_{IV,i}(r_3, \theta) = A_{III,i}(r_3, \theta), \quad (25)$$

$$H_{IV,\theta,i}(r_3, \theta) = H_{III,\theta,i}(r_3, \theta). \quad (26)$$

The eight interface conditions (19)–(26) permit to determine 21 equations with 21 unknowns for a given number of harmonics for n , m , and k .

For double-layer winding with upper and lower layer coils, the interface conditions (19)–(24) are the same. The additional conditions are as follows.

The interface conditions between Regions IV and VI at $r = r_3$ are

$$A_{IV,i}(r_3, \theta) = A_{VI,i}(r_3, \theta) \quad (27)$$

$$H_{IV,\theta,i}(r_3, \theta) = H_{VI,\theta,i}(r_3, \theta). \quad (28)$$

The interface conditions between Regions III and VI at $r = r_5$ are

$$A_{VI,i}(r_5, \theta) = A_{III,i}(r_5, \theta) \quad (29)$$

$$H_{VI,\theta,i}(r_5, \theta) = H_{III,\theta,i}(r_5, \theta). \quad (30)$$

In this case, there are 10 interface conditions (19)–(24) and (27)–(30), which permit to determine 25 equations with 25 unknowns for a given number of harmonics for n , m , k , and h . Some details of the development of interface conditions are given in the Appendix.

IV. ROTOR EDDY CURRENT AND WINDING DEFINITION

The eddy-current densities induced in the solid rotor and in the shaft are, respectively, given in the complex domain by

$$J_{er}(r, \theta) = -j \cdot \omega_{rm} \cdot \sigma_1 \cdot A_{II}(r, \theta) \quad (31)$$

$$J_{es}(r, \theta) = -j \cdot \omega_{rm} \cdot \sigma_2 \cdot A_V(r, \theta). \quad (32)$$

The current flowing through the solid rotor and in the shaft is, respectively, calculated by

$$I_{er} = \int_{R_1}^{R_2} \int_0^{2\pi} J_{er}(r, \theta) \cdot r \cdot dr \cdot d\theta \quad (33)$$

$$I_{es} = \int_0^{R_1} \int_0^{2\pi} J_{es}(r, \theta) \cdot r \cdot dr \cdot d\theta. \quad (34)$$

To calculate magnetic field distribution and eddy currents in each region, stator current density in the slots for three phases, four-pole single-layer winding is defined by a matrix connection between the phase current and stator slots as (for one pole)

$$C = \begin{bmatrix} 1 & 1 & 1 & 0 & 0 & 0 & 0 & 0 & 0 \\ 0 & 0 & 0 & 0 & 0 & 0 & 1 & 1 & 1 \\ 0 & 0 & 0 & -1 & -1 & -1 & 0 & 0 & 0 \end{bmatrix}. \quad (35)$$

For three phases, four-pole double-layer winding, the stator current density is defined by two matrix connection between the three phase's currents and stator slots as (for one pole)

$$C1 = \begin{bmatrix} 1 & 1 & 0 & 0 & 0 & 0 & 0 & 0 & -1 \\ 0 & 0 & 0 & 0 & 0 & 1 & 1 & 1 & 0 \\ 0 & 0 & -1 & -1 & -1 & 0 & 0 & 0 & 0 \end{bmatrix} \quad (36)$$

$$C2 = \begin{bmatrix} 1 & 1 & 1 & 0 & 0 & 0 & 0 & 0 & 0 \\ 0 & 0 & 0 & 0 & 0 & 0 & 1 & 1 & 1 \\ 0 & 0 & 0 & -1 & -1 & -1 & 0 & 0 & 0 \end{bmatrix}. \quad (37)$$

When the machine is fed by sinusoidal currents and has a single-layer winding, stator current densities in the slots are defined as

$$J_i = \frac{N_c}{S} \cdot C^T \cdot I_m \cdot \left[1 \ e^{-j\frac{2\pi}{3}} \ e^{j\frac{2\pi}{3}} \right] \quad (38)$$

where $S = c \cdot (r_4^2 - r_3^2)/2$ is the area of the slot, N_c is the number of conductors in the slot, and I_m is the stator phase peak current.

For three phase machines fed by sinusoidal currents and with double-layer winding, stator current density in the slots is defined as

$$J_{1i} = \frac{N_c}{2 \cdot S'} \cdot C1^T \cdot I_m \cdot \left[1 \ e^{-j\frac{2\pi}{3}} \ e^{j\frac{2\pi}{3}} \right] \quad (39)$$

$$J_{2i} = \frac{N_c}{2 \cdot S'} \cdot C2^T \cdot I_m \cdot \left[1 \ e^{-j\frac{2\pi}{3}} \ e^{j\frac{2\pi}{3}} \right] \quad (40)$$

where S' is the area of a coil and $N_c/2$ the number of conductors of one coil in the slot.

V. CIRCUIT MODEL PARAMETERS IDENTIFICATION, STATOR CURRENT, AND TORQUE

According to Maxwell stress tensor method, the electromagnetic torque T_{em} is computed using the analytical expression

$$T_{em} = \frac{L_u \cdot R_g^2}{2\mu_0} \cdot \int_0^{2\pi} \Re \{ B_{I,r}(R_g, \theta) B_{I,\theta}^*(R_g, \theta) \} \cdot d\theta \quad (41)$$

where $R_g = (R_2 + R_3)/2$ is the radius of a circular path placed at the middle of the air gap, L_u is the axial length of the motor, and $B_{I,r}(R_g, \theta)$ & $B_{I,\theta}(R_g, \theta)$ are, respectively, the radial and tangential components of the magnetic flux density in the middle of air gap determined from (8) and (9). It is noted that $B_{I,\theta}^*(R_g, \theta)$ is the complex conjugate of $B_{I,\theta}(R_g, \theta)$.

For slotted structures, the method based on Stokes theorem using the magnetic vector potential in the stator slots with single-layer winding is used for the calculation of slots flux as

$$\varphi_i = \frac{Lu}{S} \cdot \int_{\beta_i - \frac{c}{2}}^{\beta_i + \frac{c}{2}} \int_{r_3}^{r_4} A_{III,i}(r, \theta) \cdot r \cdot dr \cdot d\theta \quad (42)$$

where $A_{III,i}(r, \theta)$ is the magnetic vector potential, which is given by (12).

The development of (42) gives

$$\varphi_i = Lu \cdot C_{i,0} - \frac{\mu_0 \cdot L_u \cdot J_i}{8} \cdot r_4^2 \cdot \frac{\left(\frac{r_3}{r_4} \right)^4 + [4 \cdot \ln(r_4) - 3] + 2 \cdot [1 - 2 \cdot \ln(r_3)] \cdot \left(\frac{r_3}{r_4} \right)^2}{\left(\frac{r_3}{r_4} \right)^2 - 1}. \quad (43)$$

The complex phase flux vector is given by

$$\begin{bmatrix} \psi_a \\ \psi_b \\ \psi_c \end{bmatrix} = N_c \cdot C^T \cdot [\varphi_1 \ \varphi_2 \ \dots \ \varphi_{Q_s-1} \ \varphi_{Q_s}]. \quad (44)$$

For double-layer winding with right and left layers, the magnetic flux of the coil with a current density J_{1i} [Fig. 2(b)] is given by

$$\varphi_{1,i} = \frac{L_u}{S'} \cdot \int_{\beta_i - \frac{c}{2} - e}^{\beta_i - \frac{c}{2} + e} \int_{r_3}^{r_4} A_{III,i}(r, \theta) \cdot r \cdot dr \cdot d\theta. \quad (45)$$

For the coil with a current density J_{2i} [Fig. 2(b)], we have

$$\varphi_{2,i} = \frac{L_u}{S'} \cdot \int_{\beta_i + \frac{c}{2} - e}^{\beta_i + \frac{c}{2} + e} \int_{r_3}^{r_4} A_{III,i}(r, \theta) \cdot r \cdot dr \cdot d\theta \quad (46)$$

where $S' = e \cdot (r_4^2 - r_3^2)/2$ is the surface of the stator slot coil.

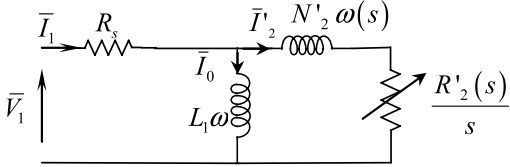


Fig. 3. EEC for the solid rotor induction motors.

For double-layer winding with upper and lower layers, the magnetic flux of the coil with a current density J_{1i} [Fig. 2(c)] is given by

$$\varphi_{1,i} = \frac{L_u}{S'} \cdot \int_{\beta_i - \frac{c}{2}}^{\beta_i + \frac{c}{2}} \int_{r_3}^{r_5} A_{VII,i}(r, \theta) \cdot r \cdot dr \cdot d\theta \quad (47)$$

where $S' = c \cdot (r_5^2 - r_3^2)/2$ is the surface of the stator slot coil.

For the coil with a current density J_{2i} [Fig. 2(c)], we have

$$\varphi_{2,i} = \frac{L_u}{S'} \cdot \int_{\beta_i - \frac{c}{2}}^{\beta_i + \frac{c}{2}} \int_{r_5}^{r_4} A_{III,i}(r, \theta) \cdot r \cdot dr \cdot d\theta \quad (48)$$

where $S' = c \cdot (r_4^2 - r_5^2)/2$ is the surface of the stator slot coil.

For the coil with current density J_{1i} , the phase flux linkage vector is given by

$$\begin{bmatrix} \psi_{1a} \\ \psi_{1b} \\ \psi_{1c} \end{bmatrix} = \frac{N_c}{2} \cdot C1^T \cdot [\varphi_{1,1} \varphi_{1,2} \dots \varphi_{1,Q_s-1} \varphi_{1,Q_s}] \quad (49)$$

For the coil with current density J_{2i} , the phase flux linkage vector is given by

$$\begin{bmatrix} \psi_{2a} \\ \psi_{2b} \\ \psi_{2c} \end{bmatrix} = \frac{N_c}{2} \cdot C2^T \cdot [\varphi_{2,1} \varphi_{2,2} \dots \varphi_{2,Q_s-1} \varphi_{2,Q_s}] \quad (50)$$

The total flux linkage per phase is

$$\begin{bmatrix} \psi_a \\ \psi_b \\ \psi_c \end{bmatrix} = \begin{bmatrix} \psi_{1a} \\ \psi_{1b} \\ \psi_{1c} \end{bmatrix} + \begin{bmatrix} \psi_{2a} \\ \psi_{2b} \\ \psi_{2c} \end{bmatrix} \quad (51)$$

The determination of the fluxes allows calculating the lumped parameters of the equivalent circuit of the induction motor. Many versions of the EEC can be proposed according to the aim of its use and the level of precision needed [11]. In this paper, a simplified EEC is considered. Neglecting the iron losses and assuming the first harmonic hypothesis, the EEC for the solid rotor induction motor shown in Fig. 3 can be considered.

In this circuit, the flux leakage inductance is lumped in the secondary branch. The electrical components of the circuit are defined as follows.

- 1) R_s is the stator resistance, which can be determined by classical analytical formula.
- 2) L_1 is the stator inductance (i.e., the magnetizing inductance).

TABLE I
PARAMETERS OF STUDIED SOLID ROTOR INDUCTION MOTOR

Parameters	Symbols	Values and unit
Relative recoil permeability of rotor	μ_{r1}	200
Relative recoil permeability of shaft	μ_{r2}	30
Number of conductors per stator slot	N_c	15
Peak phase current	I_m	20 A
Peak phase voltage	V_m	230 V
Frequency	f	50 Hz
Stator phase resistance	R_s	3.4 Ω
Number of stator slots	Q_s	36
Stator slot opening width	c	5°
Number of pole pairs	p	2
Internal radius of stator slot	r_3	63 mm
External radius of stator slot	r_4	85 mm
Coil opening width	e	2.5
Stator slot opening width	d	3°
Radius of the external stator surface	R_o	100 mm
Radius of the stator outer surface	R_3	61 mm
Radius of the rotor outer surface	R_2	60 mm
Radius of the rotor inner surface	R_1	20 mm
Air-gap length	g	1 mm
Height of a rotor	h_r	40 mm
Height of stator slot	h_s	22 mm
Axial length of the motor	L_u	200 mm
Conductivity of shaft	σ_2	1.5e6 S/m
Conductivity of solid rotor (Steel)	σ_1	5.35e6 S/m

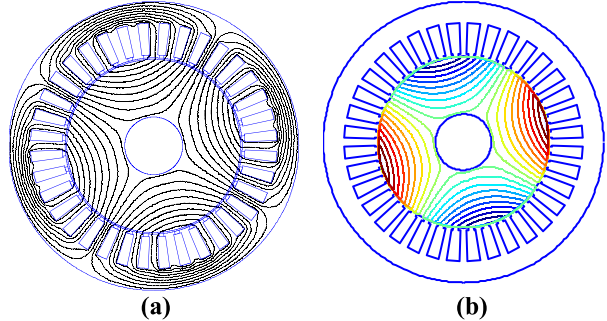


Fig. 4. Flux lines for no-load condition (i.e., $s = 0.0001$) with the single-layer winding. (a) FEM and (b) analytically $\Re e \{A_{II}(r, \theta)\}$.

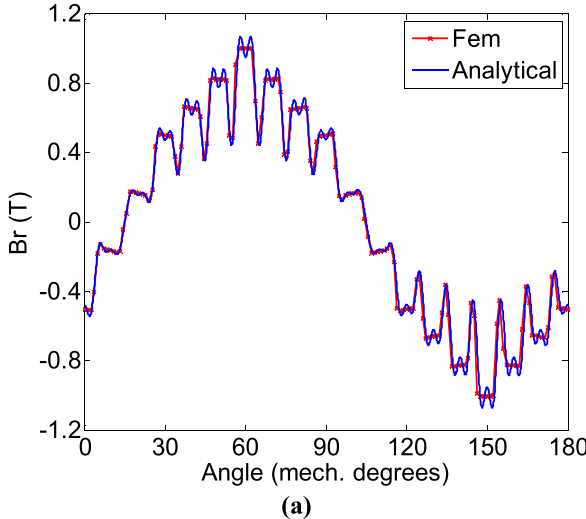
- 3) $N'_2(s)$ is the leakage inductance expressed in the rotor frame, which depends on the slip.
- 4) $R'_2(s)$ is the equivalent resistance expressed in the rotor frame, which depends on the slip.

The magnetizing inductance L_1 can be determined by performing a simulation of no-load operation (i.e., $s = 0$). It is noted that the no-load condition corresponds in our study to $s = 0.0001$. However, an analytical calculation of magnetic field at $s = 0$ can be performed easily by solving a Laplace's equation in the conducting Regions II and V. In this case, the general form of magnetic potential vector in those regions is similar to (9).

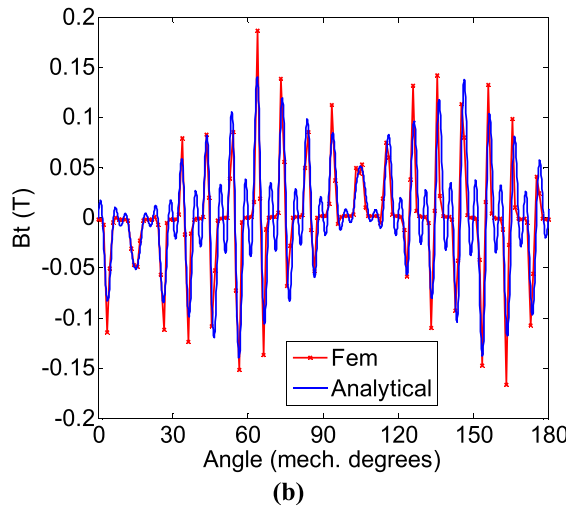
With an input three phase's currents $I = I_m \cdot [1 \ e^{-j(2\pi/3)} \ e^{j(2\pi/3)}]$, the resolution of the field equations allow determining the fluxes $[\psi_a \ \psi_b \ \psi_c]$. Therefore, we have for the phase a

$$L_1 = \frac{\psi_a}{I_m} \quad (52)$$

The calculation of the rotor parameters needs the simulation of the electromagnetic behavior for a given value of



(a)



(b)

Fig. 5. Waveforms of the (a) radial and (b) tangential components for the magnetic flux density in the middle of the air gap for no-load condition (i.e., $s = 0.0001$) with the single-layer winding: $\Re\{B_{I,r}(R_g, \theta)\}$ and $\Re\{B_{I,\theta}(R_g, \theta)\}$.

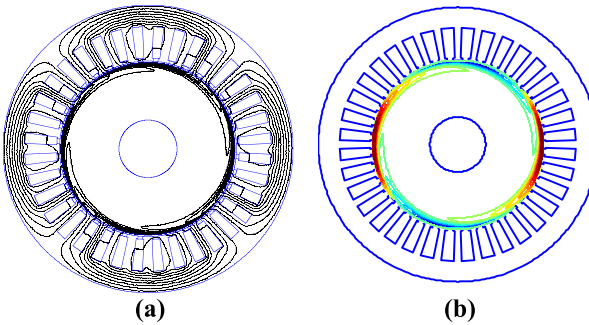
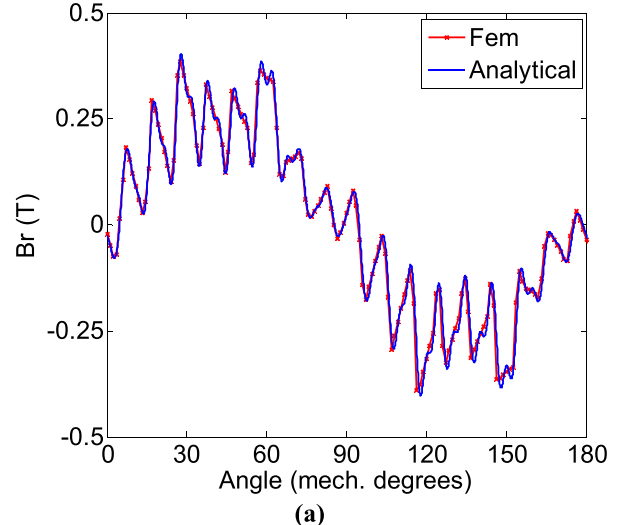
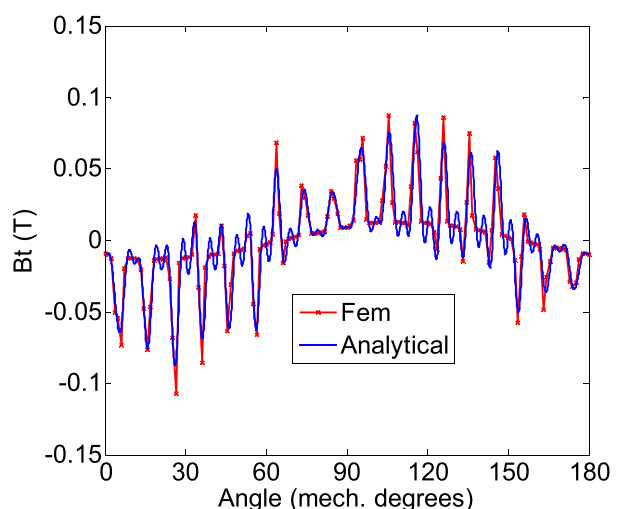


Fig. 6. Flux lines for locked rotor condition (i.e., $s = 1$) with the single-layer winding. (a) FEM and (b) analytically $\Re\{A_{II}(r, \theta)\}$.

the slip $s \neq 0$. For wound rotor induction machines, the parameters $R'_2(s)$ and $N'_2(s)$ are constant and do not depend on the rotor frequency. However, these parameters depend on the rotor frequency $\omega_{rm} = s \cdot \omega$ in the case of solid rotor induction machines due to the skin effect.



(a)



(b)

Fig. 7. Waveforms of the (a) radial and (b) tangential components for the magnetic flux density in the middle of the air gap for locked rotor condition (i.e., $s = 1$) with the single-layer winding: $\Re\{B_{I,r}(R_g, \theta)\}$ and $\Re\{B_{I,\theta}(R_g, \theta)\}$.

For load operation $s \neq 0$, the phase's currents are imposed. The resolution of the field equation allows determining the magnetic fluxes. Then, the secondary current I'_2 is determined for phase a by

$$I'_2(s) = I_m - \psi_a(s)/L_1. \quad (53)$$

The secondary impedance $Z'_2(s)$ of phase a can be calculated by

$$Z'_2(s) = \frac{j \cdot \omega \cdot \psi_a(s)}{I'_2(s)} = \frac{R'_2(s)}{s} + j \cdot N'_2(s) \cdot \omega \quad (54a)$$

$$R'_2(s) = s \cdot \Re\{Z'_2(s)\} \quad (54b)$$

$$N'_2(s) = \Im\{Z'_2(s)\}/\omega. \quad (54c)$$

This approach is adopted for the calculation of the EEC parameters by both FEM and analytical model presented in this paper. When the machine is fed with a constant three

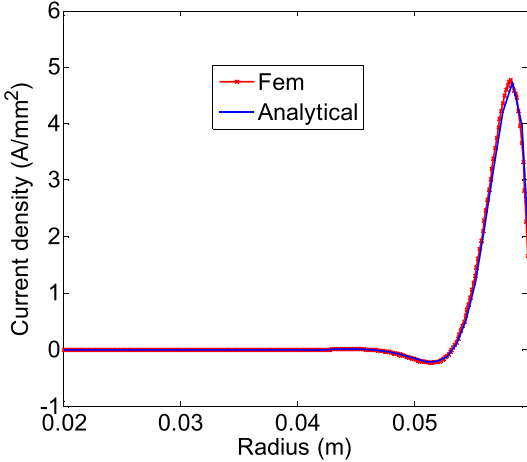


Fig. 8. Current density distribution in the solid rotor (real part) for locked rotor condition (i.e., $s = 1$) with the single-layer winding.

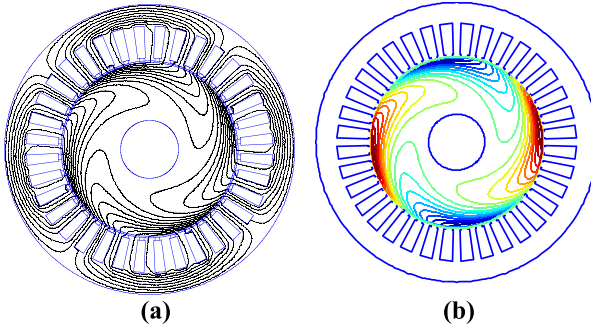


Fig. 9. Flux lines for $s = 5\%$ obtained with the single-layer winding. (a) FEM and (b) analytically $\Re \{A_{11}(r, \theta)\}$.

phase's voltage $V = V_m \cdot [1 \ e^{-j(2\pi/3)} \ e^{j(2\pi/3)}]$, the stator current of the phase a for each slip can be determined by the EEC as

$$I_1(s) = \frac{V_1}{[Z_{op}(s) + R_s]} \quad (55a)$$

$$Z_{op}(s) = \frac{j \cdot L_1 \cdot \omega \cdot \left[\frac{R'_2(s)}{s} + j \cdot N'_2(s) \cdot \omega \right]}{j \cdot L_1 \cdot \omega + \left[\frac{R'_2(s)}{s} + j \cdot N'_2(s) \cdot \omega \right]}. \quad (55b)$$

The torque-slip characteristic can be obtained analytically and by FEM. Of course, for a given stator current at a given slip (55), the torque is calculated by Maxwell stress tensor method (41). The electromagnetic torque can be also determined using the EEC. The active power in the secondary is balanced with the product of the electromagnetic torque and the synchronous speed. From the back electromotive force

$$E_1(s) = V_1 - R_s \cdot I_1(s) \quad (56)$$

the rms apparent power transmitted to the rotor is

$$S_{tr}(s) = \frac{3}{2} \cdot E_1(s) \cdot I_1^*(s) = P_{tr}(s) + j \cdot Q_{tr}(s). \quad (57)$$

The torque-slip characteristic from EEC is obtained by

$$T_{em}(s) = \frac{P_{tr}(s)}{\Omega}. \quad (58)$$

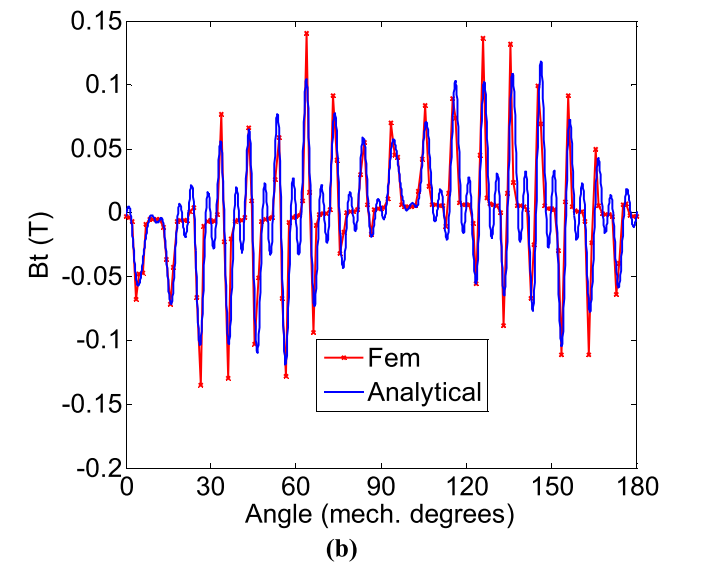
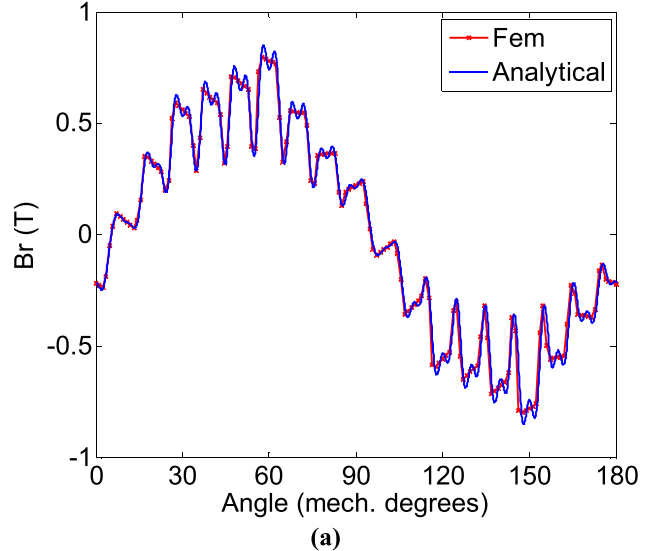


Fig. 10. Waveforms of the (a) radial and (b) tangential components for the magnetic flux density in the middle of the air gap for $s = 5\%$ with the single-layer winding: $\Re \{B_{1,r}(R_g, \theta)\}$ and $\Re \{B_{1,\theta}(R_g, \theta)\}$.

VI. ANALYTICAL RESULTS AND COMPARISON WITH FEM

The developed analytical method for solid rotor induction machines considering stator slots and tooth-tips is used for predicting magnetic field distribution, eddy currents, EEC parameters, and steady-state performances. The parameters of the studied machine are shown in Table I. The number of harmonics used is 80 for n , 4 for m , 6 for k , 6 for h , and 5 for w . For the numerical simulations, we have used 100 000 nodes and 200 000 elements.

A. Single-Layer Winding

1) *No-Load Condition:* Under no-load condition (i.e., $s = 0.0001$), Fig. 4 shows the flux lines in the machine obtained by analytical method and FEM. The radial and tangential components of the flux density distribution in the middle of the air gap are shown in Fig. 5. The effects of the stator slotting with tooth-tips can be observed. Of course,

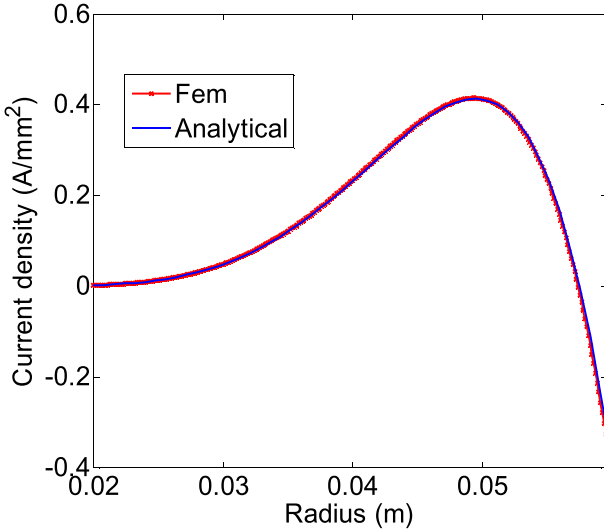


Fig. 11. Current density distribution in the solid rotor (real part) for $s = 5\%$ with the single-layer winding.

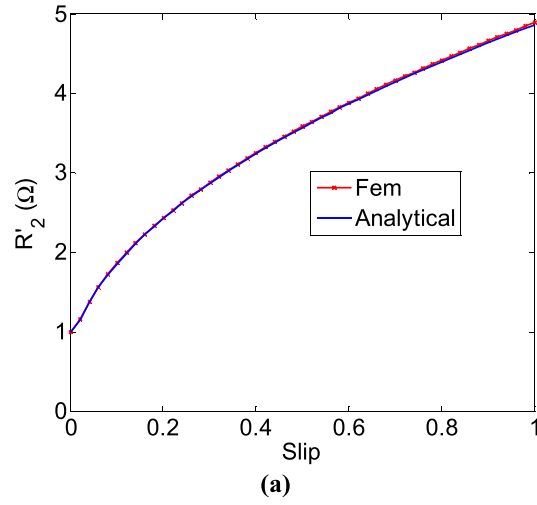


Fig. 12. Rotor parameters versus slip. (a) Equivalent resistance and (b) leakage reactance in the frame rotor.

it can be seen the nine holes per pole in the radial flux density, which corresponds to the nine slots. The eddy-current density in the rotor at no-load condition is very small and

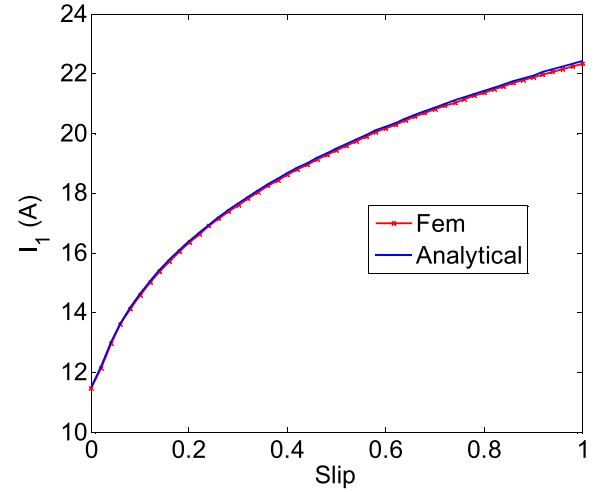


Fig. 13. RMS current-slip characteristics.

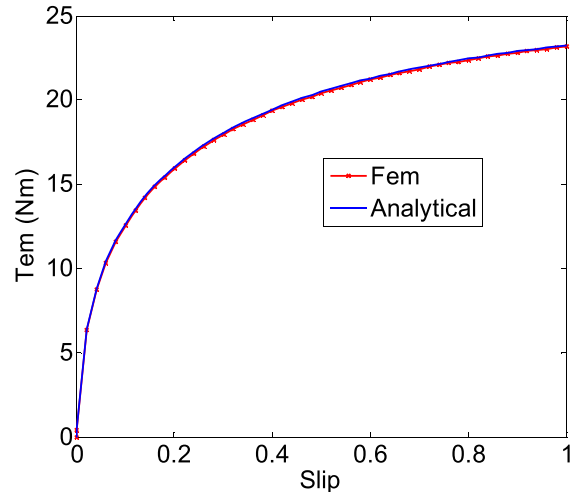


Fig. 14. Torque-slip characteristics.

therefore the flux lines penetrate deeply in the rotor. A very good agreement can be seen between the numerical and the analytical results.

2) *Locked Rotor Condition:* The flux lines distribution in the rotor are shown in Fig. 6. Due to the induced current, one can see that the magnetic field is rejected at the surface of the rotor. Fig. 7 shows the corresponding radial and tangential flux density distributions in the middle of the air gap. Compared with the no-load results, one can observe the influence of the eddy currents on both the radial and the tangential flux densities. It can be observed that the radial component of the magnetic flux density decreases.

The real part of resultant eddy-current density distribution in the solid rotor at the mechanical position $\theta = \pi/2$ is shown in Fig. 8. The current density tends to flow at the outer surface of the rotor. Magnetic field distribution and eddy currents obtained analytically are in very good accordance with FEM. It should be noticed that the eddy currents in the solid rotor, I_{er} , and shaft, I_{es} , are always zero for any electrical conductivity and slip values.

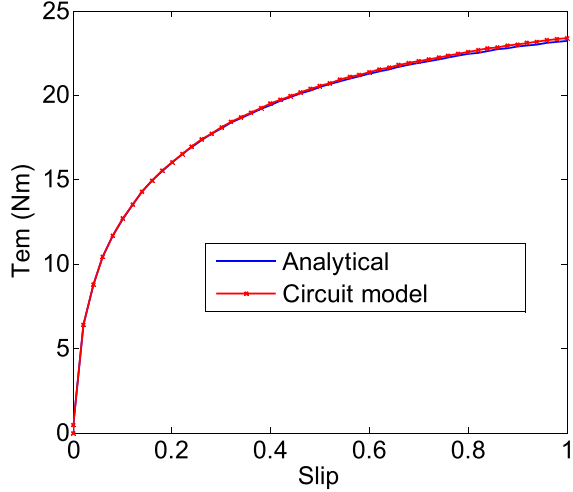
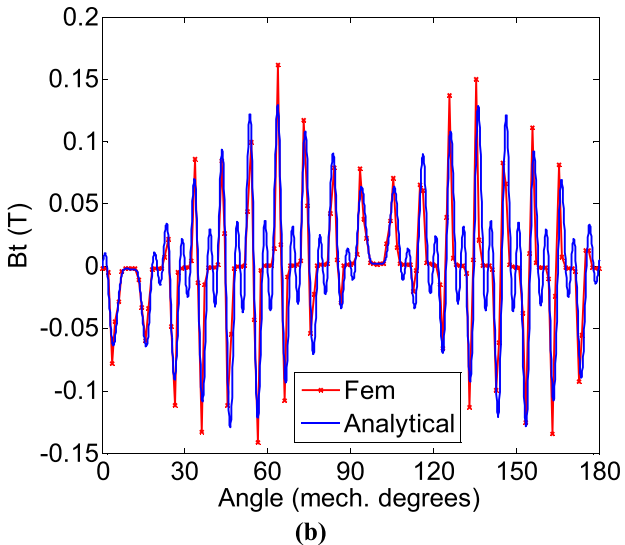
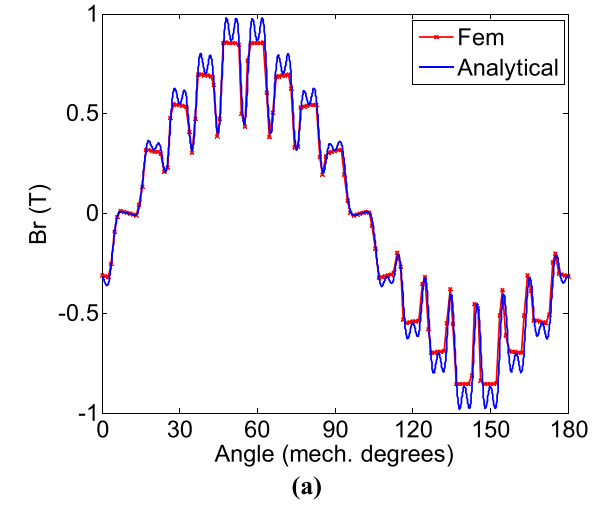
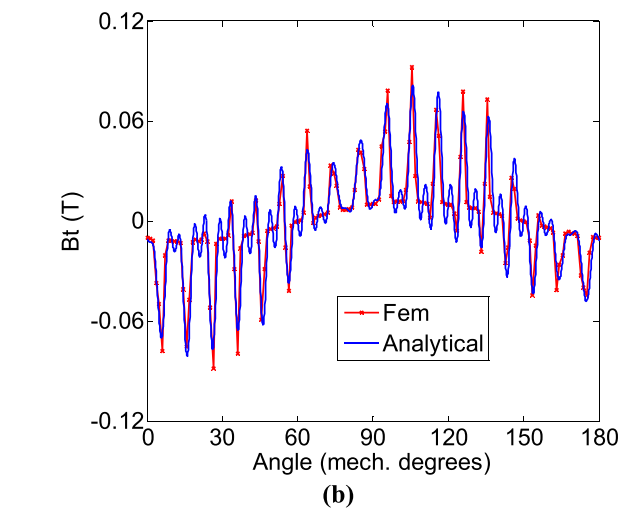
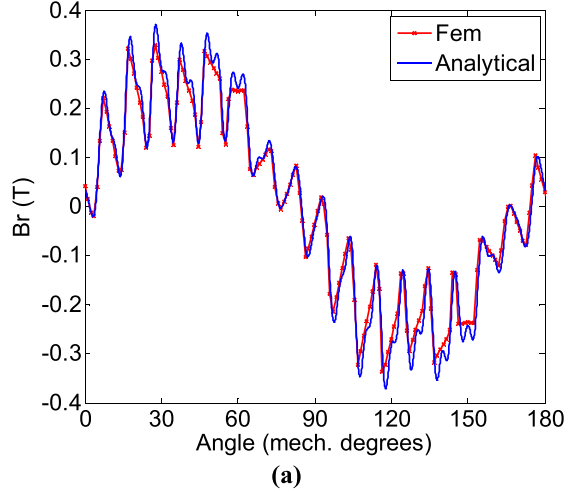


Fig. 15. Analytical and EEC torque characteristics.

Fig. 16. Waveforms of the (a) radial and (b) tangential components for the magnetic flux density in the middle of the air gap for no-load condition (i.e., $s = 0.0001$) with the double-layer winding (left and right coils): $\Re\{B_{I,r}(R_g, \theta)\}$ and $\Re\{B_{I,\theta}(R_g, \theta)\}$.

3) *Slip Equal to 5%:* For a slip of 5%, the flux lines obtained analytically and with FEM are shown in Fig. 9.

Fig. 17. Waveforms of the (a) radial and (b) tangential components for the magnetic flux density in the middle of the air gap for locked rotor condition (i.e., $s = 1$) with the double-layer winding (left and right coils): $\Re\{B_{I,r}(R_g, \theta)\}$ and $\Re\{B_{I,\theta}(R_g, \theta)\}$.

The corresponding flux density components are plotted in Fig. 10. Eddy-current density distribution at $\theta = \pi/2$ is shown in Fig. 11. All the analytical results are in a very good agreement with FEM.

4) *EEC Parameters, Stator Current, and Torque:* The values of the self-inductances calculated by FEM at $s = 0.0001$ for the three phases are $L_1 \cdot \omega = 13.73 \Omega$ while analytical model gives $L_1 \cdot \omega = 13.66 \Omega$.

Fig. 12 shows the evolution of parameters R'_2 and $N'_2 \omega$ versus the slip. It can be observed that the values of these parameters change notably with the slip. There is a very good agreement between the analytical and FEM results.

Comparison between the FEM and analytical calculation of the stator current- and torque-slip characteristics under constant voltage are shown in Figs. 13–15, respectively. It can be observed that the results obtained analytically are in a very good agreement with FEM.

B. Double-Layer Winding (Left and Right Coils)

1) *No-Load Condition:* For double-layer winding with the left and right coils, magnetic flux density components at

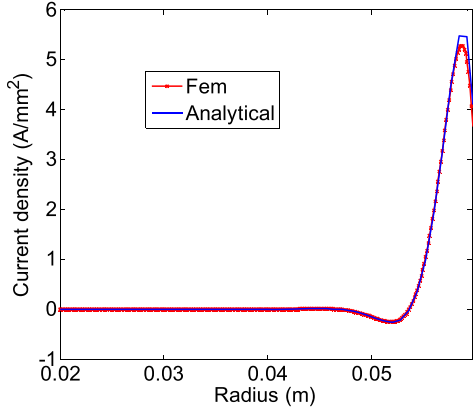


Fig. 18. Current density distribution in the solid rotor (real part) for locked rotor condition (i.e., $s = 1$) with the double-layer winding (left and right coils).

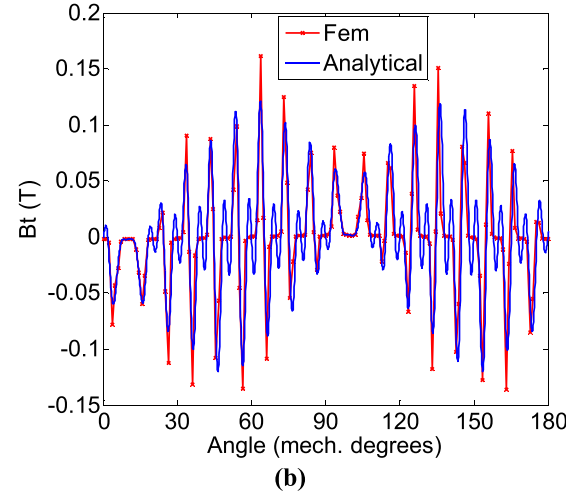
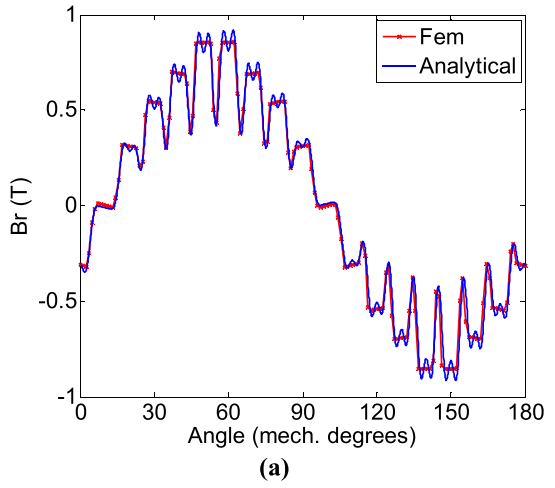


Fig. 19. Waveforms of the (a) radial and (b) tangential components for the magnetic flux density in the middle of the air gap for no-load condition (i.e., $s = 0.0001$) with the double-layer winding (upper and lower coils): $\Re\{B_{I,r}(R_g, \theta)\}$ and $\Re\{B_{I,\theta}(R_g, \theta)\}$.

the middle of the air gap is shown in Fig. 16. One can observe a small oscillation of radial and tangential flux densities predicted analytically. This is due to the limited number of harmonics used in the slots region magnetic field solution and Fourier's series expansion of slots current densities.

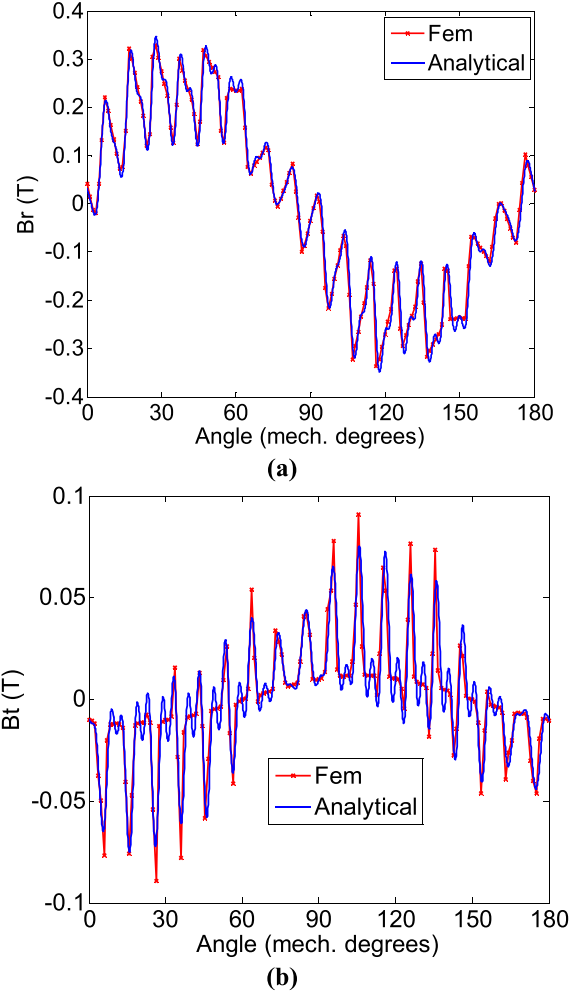


Fig. 20. Waveforms of the (a) radial and (b) tangential components for the magnetic flux density in the middle of the air gap for locked rotor condition (i.e., $s = 1$) with the double-layer winding (upper and lower coils): $\Re\{B_{I,r}(R_g, \theta)\}$ and $\Re\{B_{I,\theta}(R_g, \theta)\}$.

This limitation in the number of harmonics is due to the dimensions of subdomains, machine model dimensions, and the nature of Bessel functions in cylindrical coordinate [28]–[31]. However, the analytical results are in good agreement with those obtained with FEM.

2) Locked Rotor Condition: For locked rotor condition, flux lines are rejected at the surface of the rotor. In Fig. 17, the radial and tangential flux densities are lower than those of no-load condition. This is due to the eddy-current density distribution in the rotor, which is higher at the surface of the rotor (Fig. 18).

C. Double-Layer Winding (Upper and Lower Coils)

1) No-Load Condition: The corresponding flux density components predicted by the analytical and FEM are plotted in Fig. 19. The comparison between the analytical and numerical methods shows also a very good agreement.

2) Locked Rotor Condition: For locked rotor condition, Fig. 20 shows the flux density components. The radial flux density is lower than the no-load condition.

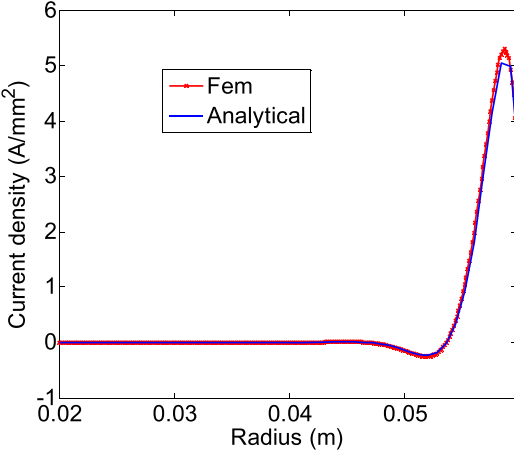


Fig. 21. Current density distribution in the solid rotor (real part) for locked rotor condition (i.e., $s = 1$).

The eddy-current density is rejected to the surface of the rotor, as observed in Fig. 21. Analytical curves are in a very good agreement with those obtained by FEM.

VII. CONCLUSION

In this paper, we have proposed a 2-D analytical method in polar coordinates for predicting magnetic field distribution, eddy currents, EEC parameters, and electromagnetic torque in the solid rotor induction machines. The developed model considers the stator slots and tooth-tips. In addition, the analysis is performed for two conducting layers, i.e., solid rotor and shaft. The whole domain is divided into five regions. Helmholtz's, Poisson's, and Laplace's equations are solved analytically using the Fourier's series and the method of separation variables. The electromagnetic torque is calculated from the magnetic field solution using Maxwell's stress tensor and EEC. Analytical model results are in a very good agreement with the ones obtained by complex FEM. Therefore, it can be used to predict rapidly the influence of the geometrical parameters, electrical conductivity, and stator winding configuration.

APPENDIX

Fourier's series coefficients of the general solution in different regions of solid rotor induction motor are determined by the resolution of a system of equations as seen above. The interface conditions are detailed as follows.

Fourier series expansion of (19) gives the following:

$$A11_0 \cdot J_0(\lambda \cdot R_1) = \left[A5_0 \cdot J_0(\alpha \cdot R_1) + \dots + A6_0 \cdot Y_0(\alpha \cdot R_1) \right] \quad (\text{A.1})$$

$$A11_n \cdot J_n(\lambda \cdot R_1) = \left[A5_n \cdot J_n(\alpha \cdot R_1) + \dots + A6_n \cdot Y_n(\alpha \cdot R_1) \right] \quad (\text{A.2})$$

$$A12_n \cdot J_n(\lambda \cdot R_1) = \left[A7_n \cdot J_n(\alpha \cdot R_1) + \dots + A8_n \cdot Y_n(\alpha \cdot R_1) \right]. \quad (\text{A.3})$$

From (20), we have

$$\frac{\alpha}{\mu_{r1}} \cdot \left[A5_0 \cdot J_1(\alpha \cdot R_1) + \dots + A6_0 \cdot Y_1(\alpha \cdot R_1) \right] = \frac{\lambda}{\mu_{r2}} \cdot A11_0 \cdot J_1(\lambda \cdot R_1) \quad (\text{A.4})$$

$$\begin{aligned} & \frac{\lambda}{\mu_{r2}} \cdot A11_n \cdot \left[-J_{n+1}(\lambda \cdot R_1) + \frac{n \cdot J_n(\lambda \cdot R_1)}{\lambda \cdot R_1} \right] \\ &= \frac{\alpha}{\mu_{r1}} \cdot A5_n \cdot \left[-J_{n+1}(\alpha \cdot R_1) + \frac{n \cdot J_n(\alpha \cdot R_1)}{\alpha \cdot R_1} \right] \\ & \dots + \frac{\alpha}{\mu_{r1}} \cdot A6_n \cdot \left[-Y_{n+1}(\alpha \cdot R_1) + \frac{n \cdot Y_n(\alpha \cdot R_1)}{\alpha \cdot R_1} \right] \end{aligned} \quad (\text{A.5})$$

$$\begin{aligned} & \frac{\lambda}{\mu_{r2}} \cdot A12_n \cdot \left[-J_{n+1}(\lambda \cdot R_1) + \frac{n \cdot J_n(\lambda \cdot R_1)}{\lambda \cdot R_1} \right] \\ &= \frac{\alpha}{\mu_{r1}} \cdot A7_n \cdot \left[-J_{n+1}(\alpha \cdot R_1) + \frac{n \cdot J_n(\alpha \cdot R_1)}{\alpha \cdot R_1} \right] \\ & \dots + \frac{\alpha}{\mu_{r1}} \cdot A8_n \cdot \left[-Y_{n+1}(\alpha \cdot R_1) + \frac{n \cdot Y_n(\alpha \cdot R_1)}{\alpha \cdot R_1} \right]. \end{aligned} \quad (\text{A.6})$$

From (21), we have

$$\left[A5_0 \cdot J_0(\alpha \cdot R_2) + \dots + A6_0 \cdot Y_0(\alpha \cdot R_2) \right] = A1_0 + A2_0 \cdot \ln(R_2) \quad (\text{A.7})$$

$$\left[A5_n \cdot J_n(\alpha \cdot R_2) + \dots + A6_n \cdot Y_n(\alpha \cdot R_2) \right] = A1_n \cdot R_2^n + A2_n \cdot R_2^{-n} \quad (\text{A.8})$$

$$\left[A7_n \cdot J_n(\alpha \cdot R_2) + \dots + A8_n \cdot Y_n(\alpha \cdot R_2) \right] = A3_n \cdot R_2^n + A4_n \cdot R_2^{-n}. \quad (\text{A.9})$$

From (22), we get

$$\frac{\alpha}{\mu_{r1}} \cdot [A5_0 \cdot J_1(\alpha \cdot R_2) + A6_0 \cdot Y_1(\alpha \cdot R_2)] = -\frac{A2_0}{R_2} \quad (\text{A.10})$$

$$\begin{aligned} & \frac{\alpha}{\mu_{r1}} \cdot A5_n \cdot \left[-J_{n+1}(\alpha \cdot R_2) + \frac{n \cdot J_n(\alpha \cdot R_2)}{\alpha \cdot R_2} \right] \\ & \dots + \frac{\alpha}{\mu_{r1}} \cdot A6_n \cdot \left[-Y_{n+1}(\alpha \cdot R_2) + \frac{n \cdot Y_n(\alpha \cdot R_2)}{\alpha \cdot R_2} \right] \\ &= n \cdot A1_n \cdot R_2^{n-1} - n \cdot A2_n \cdot R_2^{-n-1} \end{aligned} \quad (\text{A.11})$$

$$\begin{aligned} & \frac{\alpha \cdot A7_n}{\mu_{r1}} \cdot \left[-J_{n+1}(\alpha \cdot R_2) + \frac{n \cdot J_n(\alpha \cdot R_2)}{\alpha \cdot R_2} \right] \\ & \dots + \frac{\alpha \cdot A8_n}{\mu_{r1}} \cdot \left[-Y_{n+1}(\alpha \cdot R_2) + \frac{n \cdot Y_n(\alpha \cdot R_2)}{\alpha \cdot R_2} \right] \\ &= n \cdot A3_n \cdot R_2^{n-1} - n \cdot A4_n \cdot R_2^{-n-1}. \end{aligned} \quad (\text{A.12})$$

Development of (23) gives

$$A9_{i,0} + A10_{i,0} \cdot \ln(R_3) = \frac{1}{d} \cdot \int_{\beta_i - \frac{d}{2}}^{\beta_i + \frac{d}{2}} A_I(R_3, \theta) \cdot d\theta \quad (\text{A.13})$$

$$\begin{aligned} & A9_{i,m} \cdot R_3^{-\frac{m\pi}{d}} + A10_{i,m} \cdot R_3^{\frac{m\pi}{d}} \\ &= \frac{2}{d} \cdot \int_{\beta_i - \frac{d}{2}}^{\beta_i + \frac{d}{2}} A_I(R_3, \theta) \cdot \cos\left(\frac{m\pi}{d} \cdot \left(\theta - \beta_i + \frac{d}{2}\right)\right) \cdot d\theta. \end{aligned} \quad (\text{A.14})$$

From (24), we have

$$\begin{aligned} \frac{A2_0}{R_3} &= \frac{d}{2\pi \cdot R_3} \cdot \sum_{i=1}^{Q_s} A10_{i,0}, \\ &\quad - \frac{n}{\mu_0} \cdot \left(A3_n \cdot R_3^{n-1} + A4_n \cdot R_3^{-n-1} \right) \end{aligned} \quad (\text{A.15})$$

$$= \frac{1}{\pi} \cdot \sum_{i=1}^{Q_s} \int_{\beta_i - \frac{d}{2}}^{\beta_i + \frac{d}{2}} H_{IV,\theta,i}(R_3, \theta) \cdot \sin(n \cdot \theta) \cdot d\theta \quad (\text{A.16})$$

$$\begin{aligned} &- \frac{n}{\mu_0} \cdot \left(A1_n \cdot R_3^{n-1} + A2_n \cdot R_3^{-n-1} \right) \\ &= \frac{1}{\pi} \cdot \sum_{i=1}^{Q_s} \int_{\beta_i - \frac{d}{2}}^{\beta_i + \frac{d}{2}} H_{IV,\theta,i}(R_3, \theta) \cdot \cos(n \cdot \theta) \cdot d\theta. \end{aligned} \quad (\text{A.17})$$

Equation (25) gives

$$A9_{i,0} + A10_{i,0} \cdot \ln(r_3) = \frac{1}{d} \cdot \int_{\beta_i - \frac{d}{2}}^{\beta_i + \frac{d}{2}} A_{III,i}(r_3, \theta) \cdot d\theta \quad (\text{A.18})$$

$$\begin{aligned} &A9_{i,m} \cdot r_3^{-\frac{m\pi}{d}} + A10_{i,m} \cdot r_3^{\frac{m\pi}{d}} \\ &= \frac{2}{d} \cdot \int_{\beta_i - \frac{d}{2}}^{\beta_i + \frac{d}{2}} A_{III,i}(r_3, \theta) \cdot \cos\left(\frac{m\pi}{d} \cdot \left(\theta - \beta_i + \frac{d}{2}\right)\right) \cdot d\theta \end{aligned} \quad (\text{A.19})$$

where $A_{III,i}(r_3, \theta)$ is given by (12).

From (26), we have

$$\mu_0 \cdot \frac{J_i}{2} \cdot r_4^2 \cdot \left[1 - \left(\frac{r_3}{r_4} \right)^2 \right] = \frac{d}{c} \cdot A10_{i,0} \quad (\text{A.20})$$

$$\begin{aligned} &\frac{1}{\mu_0} \cdot \frac{k\pi}{c} \cdot C_{i,k} \cdot r_3^{-\frac{k\pi}{c}-1} \cdot \left[1 - \left(\frac{r_3}{r_4} \right)^{2\frac{k\pi}{c}} \right] \\ &= \frac{2}{c} \cdot \int_{\beta_i - \frac{d}{2}}^{\beta_i + \frac{d}{2}} H_{IV,\theta,i}(r_3, \theta) \cdot \cos\left(\frac{k\pi}{c} \cdot \left(\theta - \beta_i + \frac{c}{2}\right)\right) \cdot d\theta. \end{aligned} \quad (\text{A.21})$$

For double-layer winding with left and right coils, the interface conditions (19)–(25) are the same as for single-layer winding with $A_{III,i}(r_3, \theta)$ given by (14). The condition (26) is modified as

$$\mu_0 \cdot \frac{J_{i,0}}{2} \cdot r_4^2 \cdot \left[1 - \left(\frac{r_3}{r_4} \right)^2 \right] = \frac{d}{c} \cdot A10_{i,0} \quad (\text{A.22})$$

$$\begin{aligned} &\frac{1}{\mu_0} \cdot \frac{k\pi}{c} \cdot C_{i,k} \cdot r_3^{-\frac{k\pi}{c}-1} \cdot \left[1 - \left(\frac{r_3}{r_4} \right)^{2\frac{k\pi}{c}} \right] \\ &\quad \dots + \frac{1}{\mu_0} \cdot \left(\frac{k\pi}{c} \cdot G_{i,k} \cdot r_3^{\frac{k\pi}{c}-1} - 2 \cdot r_3 \cdot F_{i,k} \right) \\ &= \frac{2}{c} \cdot \int_{\beta_i - \frac{d}{2}}^{\beta_i + \frac{d}{2}} H_{IV,\theta,i}(r_3, \theta) \cdot \cos\left(\frac{k\pi}{c} \cdot \left(\theta - \beta_i + \frac{c}{2}\right)\right) \cdot d\theta. \end{aligned} \quad (\text{A.23})$$

For double-layer winding with upper and lower coils, the interface conditions (21)–(24) are the same as for single-layer winding. The development of additional conditions is as follows. From (27), we have

$$A9_{i,0} + A10_{i,0} \cdot \ln(r_3) = \frac{1}{d} \cdot \int_{\beta_i - \frac{d}{2}}^{\beta_i + \frac{d}{2}} A_{VI,i}(r_3, \theta) \cdot d\theta \quad (\text{A.24})$$

$$\begin{aligned} &A9_{i,m} \cdot r_3^{-\frac{m\pi}{d}} + A10_{i,m} \cdot r_3^{\frac{m\pi}{d}} \\ &= \frac{2}{d} \cdot \int_{\beta_i - \frac{d}{2}}^{\beta_i + \frac{d}{2}} A_{VI,i}(r_3, \theta) \cdot \cos\left(\frac{m\pi}{d} \cdot \left(\theta - \beta_i + \frac{d}{2}\right)\right) \cdot d\theta. \end{aligned} \quad (\text{A.25})$$

From (28), we have

$$\left(C2_{i,0} - \frac{1}{2} \cdot \mu_0 \cdot J1_i \cdot r_3^2 \right) = \frac{d}{c} \cdot A10_{i,0} \quad (\text{A.26})$$

$$\begin{aligned} &\frac{1}{\mu_0} \cdot \frac{h\pi}{c} \cdot \frac{1}{r_3} \cdot \left(C1_{i,h} \cdot r_3^{-\frac{h\pi}{c}} - C2_{i,h} \cdot r_3^{\frac{h\pi}{c}} \right) \\ &= \frac{2}{c} \cdot \int_{\beta_i - \frac{d}{2}}^{\beta_i + \frac{d}{2}} H_{IV,\theta,i}(r_3, \theta) \cdot \cos\left(\frac{h\pi}{c} \cdot \left(\theta - \beta_i + \frac{c}{2}\right)\right) \cdot d\theta. \end{aligned} \quad (\text{A.27})$$

Equation (29) development gives two equations as follows:

$$\begin{aligned} &C2_{i,0} \cdot \ln(r_5) - \frac{1}{4} \cdot \mu_0 \cdot J1_i \cdot r_5^2 + C1_{i,0} \\ &= \frac{1}{c} \cdot \int_{\beta_i - \frac{c}{2}}^{\beta_i + \frac{c}{2}} A_{III,i}(r_5, \theta) \cdot d\theta \end{aligned} \quad (\text{A.28})$$

$$C1_{i,h} \cdot r_5^{-\frac{h\pi}{c}} + C2_{i,h} \cdot r_5^{\frac{h\pi}{c}} = 0. \quad (\text{A.29})$$

From (30), we have

$$J2_i \cdot r_4^2 \cdot \left[\left(\frac{r_5}{r_4} \right)^2 - 1 \right] = -\frac{2}{\mu_0} \cdot C2_{i,0} + J1_i \cdot r_5^2 \quad (\text{A.30})$$

$$\frac{1}{\mu_0} \cdot \frac{k\pi}{c} \cdot C_{i,k} \cdot r_5^{-\frac{k\pi}{c}-1} \cdot \left[1 - \left(\frac{r_5}{r_4} \right)^{2\frac{k\pi}{c}} \right] = 0. \quad (\text{A.31})$$

REFERENCES

- [1] J. Pyrhönen, J. Nerg, P. Kurronen, and U. Lauber, "High-speed high-output solid-rotor induction-motor technology for gas compression," *IEEE Trans. Ind. Electron.*, vol. 57, no. 1, pp. 272–280, Jan. 2010.
- [2] E. Vassent, G. Meunier, and A. Foglia, "Simulation of induction machines using complex magnetodynamic finite element method coupled with the circuit equations," *IEEE Trans. Magn.*, vol. 27, no. 5, pp. 4246–4249, Sep. 1991.
- [3] P. Zhou, J. Gilmore, Z. Badics, and Z. J. Cendes, "Finite element analysis of induction motors based on computing detailed equivalent circuit parameters," *IEEE Trans. Magn.*, vol. 34, no. 5, pp. 3499–3502, Sep. 1998.
- [4] K. Yamazaki, "Comparison of induction motor characteristics calculated from electromagnetic field and equivalent circuit determined by 3D FEM," *IEEE Trans. Magn.*, vol. 36, no. 4, pp. 1881–1885, Jul. 2000.

- [5] R. Ibtiouen, R. Kechroud, O. Touhami, and S. Mekhtoub, "Complex finite element analysis of a solid rotor induction motor," in *Proc. IEEE IEMDC*, Jun. 2003, pp. 1606–1610.
- [6] L. T. Ergene and S. J. Salon, "Determining the equivalent circuit parameters of canned solid-rotor induction motors," *IEEE Trans. Magn.*, vol. 41, no. 7, pp. 2281–2286, Jul. 2005.
- [7] Y. Hu, J. Chen, and X. Ding, "Analysis and computation on magnetic field of solid rotor induction motor," *IEEE Trans. Appl. Supercond.*, vol. 20, no. 3, pp. 1844–1847, Jun. 2010.
- [8] A. S. Vizhi, S. Nagarajan, and S. Ramareddy, "Detection and analysis of broken bar in three phase squirrel cage induction motor using FEM," in *Proc. ICCEET*, Mar. 2012, pp. 40–50.
- [9] B. Ge, D. Sun, W. Wu, and F. Z. Peng, "Winding design, modeling, and control for pole-phase modulation induction motors," *IEEE Trans. Magn.*, vol. 49, no. 2, pp. 898–911, Feb. 2013.
- [10] D. Dolinar, R. de Weerdt, R. Belmans, and E. M. Freeman, "Calculation of two-axis induction motor model parameters using finite elements," *IEEE Trans. Energy Convers.*, vol. 12, no. 2, pp. 133–142, Jun. 1997.
- [11] P. Alger, *Induction Machines, Their Behavior and Uses*. New York, NY, USA: Gordon and Breach, 1995.
- [12] D. A. Lowther and P. P. Silvester, *Computer-Aided Design in Magnetics*. Berlin, Germany: Springer-Verlag, 1986.
- [13] A. Yahiaoui and F. Bouillaud, "2D and 3D numerical computation of electrical parameters of an induction motor," *IEEE Trans. Magn.*, vol. 30, no. 5, pp. 3690–3692, Sep. 1994.
- [14] S. Williamson and J. W. Ralph, "Finite-element analysis of an induction motor fed from a constant-voltage source," *IEE Proc. B, Elect. Power Appl.*, vol. 130, no. 1, pp. 18–24, Jan. 1983.
- [15] M. Jagieta, J. Bumby, and E. Spooner, "Time-domain and frequency-domain finite element models of a solid-rotor induction/hysteresis motor," *IET Elect. Power Appl.*, vol. 4, no. 3, pp. 185–197, Mar. 2010.
- [16] M. Mirzayee, M. Mirsalim, H. Gholizad, and S. J. Arani, "Combined 3D numerical and analytical computation approach for analysis and design of high speed solid iron rotor induction machines," in *Proc. 6th Int. Conf. CEM*, Apr. 2006, pp. 1–2.
- [17] M. Mirzayee, H. Mehrjerdi, and I. Tsurkerman, "Analysis of a high-speed solid rotor induction motor using coupled analytical method and reluctance networks," in *Proc. Int. Conf. Wireless Commun. Appl. Comput. Electromagn. (ACES)*, 2005, pp. 537–540.
- [18] Q. Wei, F. Yu, Z. Xi, and L. Shuo, "Analysis on electromagnetic field of an axial-flux solid aluminum rotor induction motor," in *Proc. ICEMS*, 2011, pp. 1–4.
- [19] M. R. Shah and S. B. Lee, "Optimization of shield thickness of finite-length solid rotors for eddy-current loss minimization," *IEEE Trans. Ind. Appl.*, vol. 45, no. 6, pp. 1947–1953, Nov./Dec. 2009.
- [20] D. Gerling and G. Dajaku, "Three-dimensional analytical calculation of induction machines with multilayer rotor structure in cylindrical coordinates," *Elect. Eng.*, vol. 86, no. 4, pp. 199–211, 2004.
- [21] K. R. Davey, "Analytic analysis of single- and three-phase induction motors," *IEEE Trans. Magn.*, vol. 34, no. 5, pp. 3721–3727, Sep. 1998.
- [22] M. Markovic and Y. Perriard, "An analytical solution for the torque and power of a solid-rotor induction motor," in *Proc. IEEE IEMDC*, May 2011, pp. 1053–1057.
- [23] S. Guo, L. Zhou, and T. Yang, "An analytical method for determining circuit parameter of a solid rotor induction motor," in *Proc. 15th ICEMS*, 2012, pp. 1–6.
- [24] G. Madescu, I. Boldea, and T. J. E. Miller, "An analytical iterative model (AIM) for induction motor design," in *Proc. 31st Annu. Meeting IAS*, 1996, pp. 566–573.
- [25] J. F. Gieras and J. Saari, "Performance calculation for a high-speed solid-rotor induction motor," *IEEE Trans. Ind. Electron.*, vol. 59, no. 6, pp. 2689–2700, Jun. 2012.
- [26] V. Räisänen, S. Suuriniemi, S. Kurz, and L. Kettunen, "Rapid computation of harmonic eddy-current losses in high-speed solid-rotor induction machines," *IEEE Trans. Energy Convers.*, vol. 28, no. 3, pp. 782–790, Sep. 2013.
- [27] F. Dubas and C. Espanet, "Analytical solution of the magnetic field in permanent-magnet motors taking into account slotting effect: No-load vector potential and flux density calculation," *IEEE Trans. Magn.*, vol. 45, no. 5, pp. 2097–2109, May 2009.
- [28] B. L. J. Gysen, K. J. Meessen, J. J. H. Paulides, and E. A. Lomonova, "General formulation of the electromagnetic field distribution in machines and devices using Fourier analysis," *IEEE Trans. Magn.*, vol. 46, no. 1, pp. 39–52, Jan. 2010.
- [29] K. Boughrara, R. Ibtiouen, and T. Lubin, "Analytical prediction of magnetic field in parallel double excitation and spoke-type permanent-magnet machines accounting for tooth-tips and shape of polar pieces," *IEEE Trans. Magn.*, vol. 48, no. 7, pp. 2121–2137, Jul. 2012.
- [30] K. Boughrara, T. Lubin, and R. Ibtiouen, "General subdomain model for predicting magnetic field in internal and external rotor multiphase flux-switching machines topologies," *IEEE Trans. Magn.*, vol. 49, no. 10, pp. 5310–5325, Oct. 2013.
- [31] F. Dubas and A. Rahideh, "Two-dimensional analytical permanent-magnet eddy-current loss calculations in slotless PMSM equipped with surface-inset magnets," *IEEE Trans. Magn.*, vol. 50, no. 3, Mar. 2014, Art. ID 6300320.
- [32] D. C. Meeker. (2009, Apr. 1). *Finite Element Method Magnetics Ver. 4.2*. [Online]. Available: <http://www.femm.info>

Kamel Boughrara was born in Algiers, Algeria, in 1969. He received the Engineer Diploma degree from École Nationale Polytechnique, Algiers, in 1994, and the Magister degree from the University of Sciences and Technology Houari Boumediene, Bab Ezzouar, in 1997, and the Doctorat d'Etat degree from École Nationale Polytechnique, in 2008.

He is currently a Lecturer with the Laboratoire de l'Energie et des Systèmes Intelligents, Université de Khemis Miliana, Algiers. His current research interests include modeling and control of electrical machines.

Frédéric Dubas was born in Vesoul, France, in 1978. He received the Degree from the University of Franche-Comté (UFC), Vesoul and Belfort, in 2002, and the Ph.D. degree from UFC, Belfort, in 2006, on the subject of the design and the optimization of high-speed surface-mounted permanent magnet motor for the drive of a fuel cell air-compressor.

He is currently an Associate Professor with the Franche-Comté Electronique, Mécanique, Thermique et Optique - Sciences et Technologies (FEMTO-ST) Institute/ENERGY Department, Besançon, France. He works with ALSTOM Transports, Ornans, and RENAULT, Guyancourt, on the modeling, design, and optimization of electrical systems, and, in particular, induction and permanent-magnet synchronous (radial and/or axial flux) machines, creative problem solving, and electrical propulsion/traction. He has authored over 50 refereed publications and holds a patent about the manufacturing of axial-flux PM machines with flux-focusing.

Dr. Dubas was a recipient of the Prize Paper Awards at the IEEE Conference Vehicle Power and Propulsion Conference in 2005.

Rachid Ibtiouen received the Ph.D. degree in electrical engineering from Ecole Nationale Polytechnique (ENP), Algiers, Algeria, and the Institut National Polytechnique de Lorraine, Nancy, France, in 1993.

He integrated the Groupe de Recherche en Electrotechnique et Electronique de Nancy, Nancy, from 1988 to 1993. From 1993 to 2011, he was an Expert Member of the Committee of Evaluation of the University Projects of Research with the Ministry of the Algerian Higher Education. From 2005 to 2013, he was the Director of the Laboratoire de Recherche en Electrotechnique, ENP. He is currently the Head of the Department of Electrical Engineering, ENP. He is currently a Professor and the Associated Director of Research with ENP. His current research interests include modeling electric systems and drives, in particular, electrical machines.